Cell Force Microscopy on Elastic Layers of Finite Thickness

Rudolf Merkel, Norbert Kirchgeßner, Claudia M. Cesa, and Bernd Hoffmann

Institute of Bio- and Nanosystems, Research Centre Jülich, Jülich, Germany

ABSTRACT   Forces applied by cells to substrates can be measured using soft substrates with embedded displacement markers. Traction forces are retrieved from microscopic images by determining the displacements of these markers and fitting the generating forces. Here we show that using elastic films of 5–10-μm thickness one can improve the spatial resolution of the technique. To this end we derived explicit equations for the mechanical response of an elastic layer of finite thickness to point forces. Moreover, these equations allow highly accurate force measurements on eukaryotic cells on films where finite thickness effects are relevant (below ~60 μm).

INTRODUCTION

Most animal cells survive only if they are adhered to substrates or other cells. For this reason cell adhesion has been intensively studied. At present a wealth of facts is known on the molecules causing cell adhesion and on their regulation as well as supramolecular organization. Interestingly, cell adhesion molecules form well-defined aggregates within the cell substrate contact area. Focal adhesion sites, podosomes, and hemidesmosomes are prominent examples (1–4).

An outstanding biological function of such complexes is the transmission of mechanical force. Obviously, techniques to determine these forces at the level of single contacts are needed to investigate this function. Here a first breakthrough was the wrinkling assay of Harris (5). In this assay cells are cultivated on a thin elastic lamella that forms folds due to cell forces. However, quantitative evaluation of the observed patterns is very difficult because wrinkling is a highly nonlinear process. Later on, wrinkling was effectively suppressed by using elastic layers bonded to microscope coverslips (cf. Fig. 1) (6–10).

In such experiments the displacement field of the surface of the elastic medium is determined directly. If the force distribution is known, this field can be easily calculated by convoluting the force distribution with the appropriate Greens' tensor. Thus, for traction force microscopy the Greens' tensor plays the role of an instrumental resolution function. Its spatial decay limits the obtainable spatial resolution of the technique.

Evaluating data from traction force microscopy amounts to unfolding the Greens' tensor and the unknown force distribution. This is a classical example for an inverse problem. This class of problems is numerically ill-posed (11). In the literature it was convincingly shown that regularized, nonlinear data fit routines can be used to calculate force distributions from displacement fields (12,13). In experiments the displacement field is determined with a certain uncertainty at discrete locations. Due to these two limitations the outcome of any unfolding algorithm will be of restricted spatial resolution. In other words, the forces due to focal adhesions in close proximity will tend to be averaged by the evaluation procedure. The exact amount of smoothing is difficult to estimate because choosing the regularization parameter is in essence a subjective procedure. As an alternative to regularized least squares fitting unfolding can be also performed in Fourier space (10). Here as well some smoothing is necessary to overcome high frequency noise. No matter what technique is used, a more rapidly decaying instrument function will result in better separation of the contributions of different focal adhesions.

The resolution problem in traction force microscopy is rather severe because the Greens' tensor of an elastic half-space decays only like the inverse of the distance. In this publication we will show that finite thickness of the elastic layer leads to a more rapid decay and therefore to a better spatial resolution of traction force microscopy on moderately thin elastic films.

This publication is organized as follows. First we will give explicit expressions for the Greens' tensor of a point force acting on an elastic layer of finite thickness that is bonded to a rigid substrate and discuss the shape of the solutions. Then we will describe prototype experiments where we applied point forces to elastic layers and compare the resulting deformation fields with our calculations. Finally we will apply our results to traction force experiments on living cells and discuss our findings.

MATERIALS AND METHODS

Mathematics and digital image processing

Many symbolic calculations were supported by Maple (Version 9.51, Maplesoft, Waterloo, Ontario, Canada). Numerical routines for integrating the final solutions, for digital image processing, and for data fitting were programmed in MatLab (Release 14, Mathworks, Natick, MA). Image processing routines for micropatterned substrates exhibiting a regular grid of microdimples are described in detail in Cesa et al. (14). In short, we correlated the image of
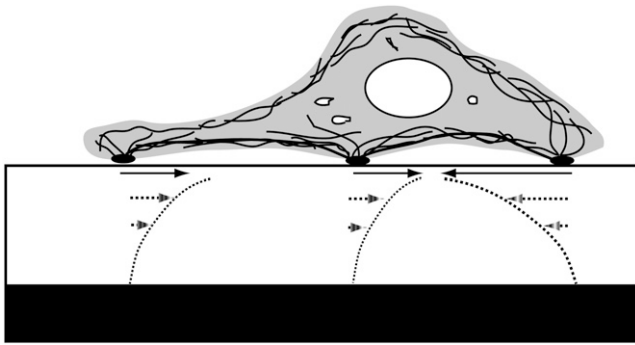
FIGURE 1 The basic principle of traction force microscopy. A cell (*gray*) adheres to an elastic substrate predominantly at specific locations (*black ellipses*). Mechanical forces (*solid arrows*) result in deformations of the substrate (*dotted arrows*) that decay in normal direction (*dotted lines*) and in tangential direction (not shown). The elastic film is supported by a rigid substrate, in general a microscope coverslip (*black*).

a small region around each dot of the microstructure in the images before and after deformation. The maximum of the correlation yielded the position of the point. These values exhibited an uncertainty of ~30 nm.

Surfaces exhibiting fluorescent microbeads in a random pattern had to be treated differently. In a first step, a fluorescence micrograph of an area enclosing a cell was analyzed. This image is called the original image. Here individual microbeads were localized by cross correlation with an arbitrarily chosen microbead as template. In a second step, this cell was removed by trypsination. Subsequently, a reference image of the same region was taken where microbead locations were determined by the same techniques. Judged from cell free areas the statistical uncertainty of the bead displacements was 10 nm. Displacements of beads from the first image to the second one had to be corrected for drift and erroneously assigned beads. Drift was determined from the average shift of microbeads in areas far from the cell. Especially in areas with large displacements, our algorithm sometimes failed to find the same beads in the original and the reference image. This led to apparent displacements that widely differed in magnitude and direction from neighboring ones. Such artificial displacements were discarded.

Force retrieval was performed by the algorithm of Schwarz et al. (13). This algorithm performs a regularized least squares fitting of the model function to the data (11,15). We used n discrete point forces, $\vec{f}_i$, located at the positions (x_i, y_i), to calculate the model function $\vec{u}_t$

$$\vec{u}_t(x, y) = \sum_{i=1}^{n} \vec{\vec{G}}(x - x_i, y - y_i)\vec{f}_i. \qquad (1)$$

Here $\vec{\vec{G}}$ denotes the Greens' tensor of the problem (see below). In the experiment displacements $\vec{u}_e$ of m marker particles or structures at positions (x_j, y_j) were determined. The forces $\vec{f}_i$ were chosen to minimize the merit function MF.

$$MF = \chi^2 + \lambda^2 C^2$$
$$= \sum_{j=1}^{m} \frac{(\vec{u}_t(x_j, y_j) - \vec{u}_e(x_j, y_j))^2}{\sigma_j^2} + \lambda^2 \sum_{i=1}^{n} \vec{f}_i \vec{f}_i. \qquad (2)$$

Here σ_j denotes the statistical uncertainty (standard deviation) of the data point j. For experiments on substrates with regular microstructures σ amounted to 30 nm, on microbead coated substrates σ was 10 nm. The first sum in Eq. 2, χ^2, is the familiar sum of squared deviations. Due to the structure of the Greens' tensor, minimizing the first factor alone yields fluctuating, meaningless solutions. These fluctuations are effectively damped by the constraint C, which corresponds to the second sum in Eq. 2. It penalizes solutions with high magnitudes of forces (15). The amount of regularization is tuned by the

regularization parameter λ. Choosing λ amounts to obtaining a fair compromise between erroneously fluctuating forces at too small values and excessively smoothed solutions at too high values. We varied λ and calculated the respective χ^2. Two different criteria for the selection of λ are possible: either one selects the value of λ, which yields the statistically expected value of $\chi^2 = 2(m - n)$ or one chooses λ at the position where the $\chi^2(\lambda)$ curve starts to rise significantly. In this work we used the second alternative. The respective value of λ was chosen automatically as the value that maximizes the third derivative of the $\chi^2(\lambda)$ curve. Examples will be shown below. Much more detail on this particular method of data retrieval can be found in the original work of Schwarz et al. (13). Another valuable source of information is the description of the Matlab package Regularization Tools by Hansen (15).

Preparation of elastic microstructured substrates

The preparation procedures for substrates exhibiting periodic microstructures are described in detail in Cesa et al. (14). In short, weakly cross-linked silicon elastomer was used as elastic layer (Sylgard 184, Dow Corning, Midland, MI). This material is supplied as a two-component kit consisting of base material and cross-linker. Both fluids were mixed at a ratio of 55:1 and deposited onto a silicon waver bearing a microstructure consisting of 2-μm dots arranged in a square lattice of 3.5-μm lattice constant on its surface. The polymer layer was then covered by a glass coverslip. During heat cross-linking (60°C overnight) the waver served as mold that was subsequently removed.

Microbead covered elastic substrates were produced from Sylgard for base material to cross-linker ratios of 55:1 and 45:1. In detail, FluoSpheres (100-nm diameter; Invitrogen, Carlsbad, CA) were pelleted by centrifugation and homogenized at a concentration of 5% (v/v) in the mixed but still not cross-linked polymer solution. This bead-labeled fluid was coated onto a silicon surface silanized with trichloro(1H,1H,2H,2H-perfluorooctyl)silane (Sigma-Aldrich, St. Louis, MO). Subsequently, the layer thickness was reduced to <0.5 μm by wiping with lens tissue (NeoLab, Heidelberg, Germany). After cross-linking the bead-labeled elastomer layer, unlabeled Sylgard mixture of identical ratio was overlaid. Layer thicknesses of 100 μm were produced by using spacers between the silicon surface and the coverslip. For fabrication of thin elastomer substrates, wedge-shaped elastic structures were produced. Here, an 80-μm spacer between silicon and coverslip was used only at one side of the coverslip while the other was pressed down with a paperclip. The resulting elastomer wedges exhibited defined thicknesses down to 5 μm.

Layer thicknesses were accurately determined at the positions of each cell analyzed with a confocal microscope (Zeiss LSM510 with an Axiovert 200M as base microscope; Carl Zeiss Jena, Germany). For thick elastomer layers reflection mode was used employing the 488-nm line of the Argon ion laser. Thin elastomer substrates were stained with DiD (1,1'-dioctadecyl-3,3,3',3'-tetramethylindodicarbocyanine perchlorate, 1 mM in ethanol; Molecular Probes, Eugene, OR) in 1:500 dilution in water for 16 h at 37°C and imaged with the confocal microscope using a green HeNe laser (543 nm) and a 560-nm long-pass filter. An Epiplan 50 × /0.7 lens was used for reflection analysis. In fluorescence microscopy a PlanApochromat 63 × /1.40 oil differential interference contrast objective was used. The film thicknesses were corrected for the influence of the mismatch in refractive indices between air ($n = 1.0$) or immersion oil ($n = 1.515$) and cross-linked polydimethylsiloxane ($n = 1.41$) (16). The latter value was determined by an Abbe refractometer (AR 3–6 D; A. Krüss, Hamburg, Germany). The elastomer films exhibited a Poisson ratio of 0.50 and a Young's modulus of 16 kPa for a mixing ratio of 55:1, respectively, 38 kPa for a mixing ratio of 45:1. These mechanical material parameters were determined as described in Cesa et al. (14).

Preparation of cells

Cardiac fibroblasts were isolated from 19-day-old Wistar rat embryos. In brief, CO_2 anesthetized pregnant rats were decapitated, the embryos were removed and decapitated under sterile conditions. The heart of each embryo was quickly isolated, washed in Hank's balanced salt solution ((HBSS) Sigma), cut into small pieces and repeatedly digested in a 0.5% trypsin/0.2% EDTA solution in HBSS to disintegrate the tissue. Undigested cell aggregates

were further incubated in between with 100 μl DNase solution (10,000 units/ml; Sigma). Cells were collected by centrifugation at $200 \times g$. Cells were seeded on PDMS surfaces that were coated with 2.5 μg/cm^2 human plasma fibronectin (BD Biosciences, San Jose, CA). After 50-min nonadherent cells (primarily myocytes as they adhere slower than cardiac fibroblasts) were taken away with the supernatant. Cells were maintained in F10 Ham's medium supplemented with 10% fetal bovine serum, a 1:100 dilution of an antibiotic solution (10,000 units penicillin and 10 mg/ml streptomycin in 0.9% NaCl, Sigma) and a 1:200 dilution of a solution containing insulin (1 mg/ml), transferrin (0.55 mg/ml), and sodium selenite (0.5 μg/ml) in Earle's balanced salt solution (Sigma) at 37°C and 5% CO_2 in a humidified incubator.

Light microscopy techniques

For needle tests deformation fields were examined in reflection mode using the laser scanning microscope equipped with an Epiplan $50\times$ /0.7 lens (Zeiss). Here a green HeNe laser (543 nm) was used for illumination. To minimize geometrical image distortions the scanner was calibrated before the measurements. Moreover, a very low scanning rate was used.

Live cell microscopy was performed on an inverted light microscope (Axiovert 200, Zeiss) using a PlanNeofluar $63\times$ /1.25 Ph3 Antiflex lens (Zeiss). Cells were analyzed in phase contrast as well as in reflection interference contrast microscopy (RICM). The latter allowed us to detect focal adhesion sites of cells as well as the microstructure of the elastic substrate. Cell culture conditions were maintained by means of a thermostated chamber flushed with 5% CO_2 (Incubator XL-3; Zeiss). Fluorescence of beads was excited by the 546-nm line of a mercury arc lamp (HBO100/W3 Osram, Munich, Germany) and selected by the appropriate filter set (FS-09, Zeiss). Image acquisition was performed using an ORCA ER CCD camera (Hamamatsu Photonics, Hamamatsu, Japan) and Open Box as software (version 1.77, Informationssysteme Schilling, Munich, Germany).

Theoretical considerations

The Greens' tensor for a single, elastic layer bonded to a rigid substrate

For an elastic half-space the Greens' tensor for displacements caused by point forces was solved 130 years ago by Boussinesq (17). In view of the high relevance of layered materials, e.g., in road construction or building foundations, it is astonishing that it took another 60 years until Burmister solved the case of a normal force acting on a layered material (18–20). However, lateral forces break the radial symmetry of the problem and were much more difficult to tackle. In essence, meaningful solutions could only be achieved with the advent of easy accessible computer-based numerics. For the practical implementation of the solution we found the approach of Yue and co-workers most convenient (21–24). Yue's treatment is based on a Hankel transformation of the differential equation combined with a matrix transfer technique to connect the boundary conditions at the diverse interfaces in a layered continuum. Alternatively, one could have calculated the Greens' tensor by a method based on elastic potential functions and image point loads to satisfy the boundary conditions (25).

The displacement field of the surface of an elastic medium, $\vec{u}$ is connected to the force distribution acting on this surface, $\vec{f}$, by

Here x and y symbolize the coordinates within the surface and $\vec{G}$ denotes the Greens' tensor for this mechanical problem. Please note that forces and displacements can have tangential and normal components, i.e., all vectors have three elements and the Greens' tensor is a 3×3 matrix.

Calculation of the Greens' tensor, $\vec{G}$, was the most difficult problem to be tackled in this project. Our approach was based on Yue (22) who gave an algorithm to numerically calculate the Greens' tensor for stratified media, i.e., materials consisting of several plane parallel slabs of isotropic, homogeneous, and linearly elastic materials rigidly bonded at their interfaces and to an infinitely thick underlying solid material.

Our system consists merely of one layer of elastomer bonded to a glass coverslip. For this comparably simple case the relevant equations from Yue (22) could be calculated in explicit form. The resulting expressions could be substantially simplified by assuming an infinitely stiff underlying material. This is well justified because the Young's modulus of the elastomer is typically in the range of 0.1–100 kPa, whereas a glass coverslip exhibits a Young's modulus of 73 GPa (value given by Schott AG, Mainz, Germany).

The final result is

$$\vec{G} = \begin{pmatrix} A_1 - \dfrac{x^2-y^2}{r^2}A_2 & -\dfrac{2xy}{r^2}A_2 & -\dfrac{x}{r}A_3 \\[2mm] -\dfrac{2xy}{r^2}A_2 & A_1 + \dfrac{x^2-y^2}{r^2}A_2 & -\dfrac{y}{r}A_3 \\[2mm] \dfrac{x}{r}A_3 & \dfrac{y}{r}A_3 & A_4 \end{pmatrix}. \quad (4)$$

Here $r = \sqrt{x^2+y^2}$. The terms A_i in the above tensor are given by

$$A_i = A_{i,B} + A_{i,A} \quad \text{for} \quad i \in \{1, 2, 3, 4\}, \quad (5)$$

i.e., we split the solution in the Boussinesq solution $A_{i,B}$ for an infinite layer thickness and a deviatory part $A_{i,A}$. The Boussinesq solution is given by

$$A_{1,B} = \frac{1}{4\pi\mu h}\frac{2-\sigma}{s}$$

$$A_{2,B} = -\frac{1}{4\pi\mu h}\frac{\sigma}{s}$$

$$A_{3,B} = \frac{1}{4\pi\mu h}\frac{1-2\sigma}{s}$$

$$A_{4,B} = \frac{1}{4\pi\mu h}\frac{2(1-\sigma)}{s}. \quad (6)$$

Here and in the following s denotes the scaled radius ($s = r/h$), h being the layer thickness. The elastic parameters of the layer are defined by the Poisson's number, σ, and the shear modulus, μ. The latter modulus is connected to the more familiar Young's modulus, E, via $\mu = E/(2(1 + \sigma))$.

$$A_{1,A} = -\frac{1}{2\pi\mu h}\int_0^\infty J_0(st)\Phi_1(\sigma, t)dt$$

$$\Phi_1(\sigma, t) = \frac{-\exp(-2t)}{N(1+\exp(-2t))} \times \{2(\sigma-1)t^2 + 2(1-\sigma)t + 8\sigma^3 - 20\sigma^2 + 21\sigma - 8 + [2(\sigma-3)t^2 + 2(1-\sigma)t + 8\sigma^3$$
$$- 40\sigma^2 + 48\sigma - 18] \times \exp(-2t) + [-4\sigma^2 + 11\sigma - 6] \times \exp(-4t)\} \quad (7)$$

$$\vec{u}(x, y) = \int \vec{G}(x-x', y-y')\vec{f}(x', y')dx'dy'. \quad (3)$$

$$A_{2,A} = -\frac{1}{2\pi\mu h}\int_0^\infty J_2(st)\Phi_2(\sigma, t)dt$$

$$\Phi_2(\sigma, t) = \frac{-\exp(-2t)}{N(1+\exp(-2t))} \times \{2(\sigma-1)t^2+2(1-\sigma)t+8\sigma^3-20\sigma^2+13\sigma-2+[2(\sigma+1)t^2+2(1-\sigma)t$$
$$+8\sigma^2(\sigma-1)+2] \times \exp(-2t)+[\sigma(3-4\sigma)] \times \exp(-4t)\} \tag{8}$$

$$A_{3,A} = -\frac{1}{2\pi\mu h} \int_0^\infty J_1(st)\Phi_3(\sigma, t)dt\Phi_3(\sigma, t)$$
$$= \frac{4(1-\sigma)\exp(-2t)}{N} \times \{t^2+2(2\sigma-1)(\sigma-1)\} \tag{9}$$

$$A_{4,A} = -\frac{1}{2\pi\mu h} \int_0^\infty J_0(st)\Phi_4(\sigma, t)dt$$
$$\Phi_4(\sigma, t) = \frac{2(1-\sigma)\exp(-2t)}{N} \times \{2t(t+1)+8\sigma^2$$
$$-12\sigma+5+[3-4\sigma] \times \exp(-2t)\}. \tag{10}$$

In these equations J_n denotes the Bessel function of first kind and order n (26), and the term N is given by

$$N(\sigma, t) = (3-4\sigma)\exp(-4t)+[-24\sigma+10$$
$$+4t^2+16\sigma^2]\exp(-2t)+(3-4\sigma). \tag{11}$$

All the individual terms A_i as well as $A_{i,B}$ and $A_{i,A}$ (cf. Eqs. 4 and 5) can be scaled to be functions, M_l, of only two variables via

$$\mu h A_l(r, h, \sigma, \mu) = M_l(s, \sigma), \tag{12}$$

where the index l stands for either i, (i, B), or (i, A) and we used again the scaled distance $s = r/h$.

General structure of the solution

The Greens' tensor for an elastic layer bonded to a rigid substrate can be reduced to four functions A_i. These functions depend in a trivial way on thickness and shear modulus. Thus the only nontrivial variables are the Poisson's number, σ, and the distance in the surface scaled by the thickness of the layer, $s = r/h$; see Eq. 12. In the following we will discuss the shape of these functions A_i and focus on the most important case of $\sigma = 1/2$. This value has been given for many materials used so far in traction force microscopy (7,9). The integrals in Eqs. 7–10 were numerically evaluated to an accuracy of 10^{-11}.

Let us first address the deviatory parts of the solutions, $A_{i,A}$. These functions are well behaved because the integrands in Eqs. 7–10 decay like $\exp(-2t)$ for $t \to \infty$ and are continuous functions over the full range of integration without any poles. Please note that this holds for all physically possible values of σ ($-1 \leq \sigma \leq 1/2$). For $\sigma = 0.5$ the functions $A_{i,A}$ are displayed in Fig. 2.

These solutions exhibit finite values at $s = 0$ and decay like $1/s$ for large distances. Here the deviatory parts converge to the negative of the respective terms of the Boussinesq solution resulting in a cancellation of both terms. Thus the solutions for finite layer thickness decay faster than the Boussinesq solution at large distances. However, close to the center the deviatory parts stay finite while the Boussinesq solutions diverge like $1/r$. Thus the final solutions, A_i, differ from the Boussinesq solutions mostly at larger distances; cf. Fig. 3.

One remarkable feature of the finite layer solution is that the horizontal and tangential degrees of freedom do not separate at Poisson's number 0.5.

This is formally expressed by a nonzero value of A_3; see Fig. 3. Moreover, A_2 appears to be quite well approximated by the Boussinesq solution whereas A_4 and A_3 show especially large deviations. This is expected as these two terms describe the reaction of the material to normal forces. Here the finite thickness should play a greater role as compared to shear deformations. The deviations between the finite layer solutions and the Boussinesq solutions can be best examined upon plotting the ratio of both solutions; cf. Fig. 4.

Please note that all ratios decay to zero at distances corresponding to few layer thicknesses. This shows that the deformation fields decay much faster in the finite layer case in comparison to the Boussinesq solution. Moreover, it is apparent that the Boussinesq solution approximates A_2 reasonably well at small distances. The deviation between both solutions is below 2% for $s = r/h$ below 1.3. However, the same accuracy for A_1 requires $s \leq 0.03$ and for A_4 $s \leq 0.01$. In addition, Fig. 4 shows that the general shape of the solutions does not change much by changing the Poisson's number from 1/2 to 0.3.

The major advantage of the Boussinesq solution for all practical purposes is its high computational efficiency compared to the finite layer solution. However, for many purposes approximate expressions might be sufficient. For a Poisson's number of 1/2 we find the following approximations to the finite layer solution:

$$A_1 \approx A_{1,B}(0.12\exp(-0.43s)+0.88\exp(-0.83s))$$
$$A_2 \approx A_{2,B}(1+1.22s+1.31s^{2.23})\exp(-1.25s)$$
$$A_3 \approx -0.063[\exp(-0.44s)-\exp(-2.79s)]^2$$
$$A_4 \approx A_{4,B}(1+0.46s-2.50s^{2.13})\exp(-2.18s). \tag{13}$$

The relative accuracies for A_1, A_2, and A_4 are 0.8%, 1.8%, and 2.2% of $A_{B,i}$, respectively. The accuracy of the approximation for A_3 is 2×10^{-3}.

Experimental tests of the finite layer effects

Needle tests

Microstructured elastomer films of defined thickness were mounted onto the stage of the confocal microscope. A syringe needle (22 gauge) was mounted perpendicular to the elastomer surface in a micromanipulator (MHW-3
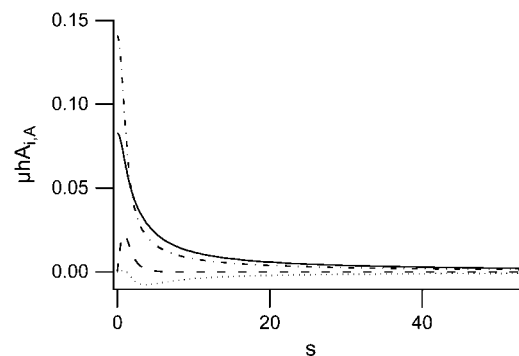

FIGURE 2 The deviatory part of the solutions, $A_{i,A}$; cf. Eqs. 5 and 7–11. The Poisson's number, σ, is 1/2. (Solid line) $A_{1,A}$; (dotted line) $A_{2,A}$; (dashed line) $A_{3,A}$; and (dash-dotted line) $A_{4,A}$.
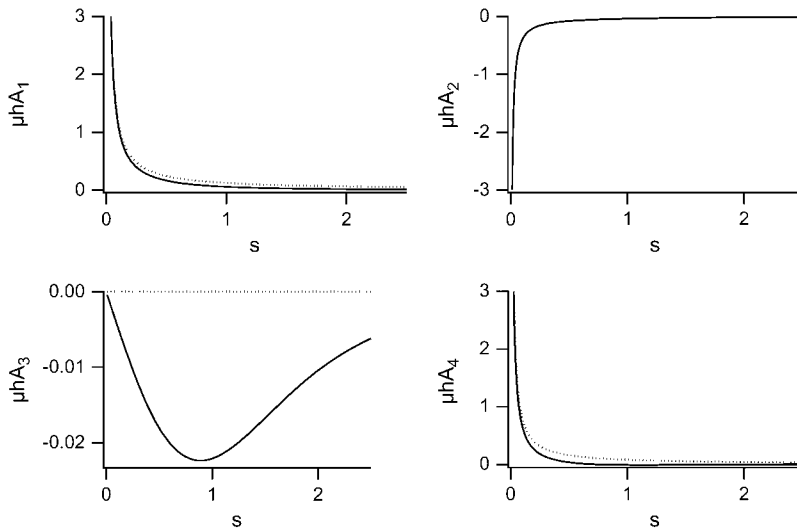
FIGURE 3 The functions A_i from Eq. 4 for Poisson's number $\sigma = 1/2$. The dotted lines denote the Boussinesq solutions, i.e., the solutions for an infinitely thick substrate. Note the different scale for A_3.

Narishige, Tokyo, Japan). The needle was gently pressed onto the substrate (indentation below 3 μm) and moved to the side. Due to adhesion between needle and substrate, the elastomer film was stably deformed upon needle translation. Micrographs of the microstructured surface were taken before and after moving the needle. The displacements of the microstructures were determined by digital image processing. An example is shown in Fig. 5.

For each of these displacement fields we fitted the generating force of the needle. In this fit we assumed a single point force in the middle of the contact zone between needle and substrate. We used the algorithm published by

FIGURE 4 The ratios between the finite layer solutions, A_i, and the Boussinesq solutions, $A_{i, B}$. (Solid line) $A_1/A_{1, B}$; (dotted line) $A_2/A_{2, B}$; (dashed line) $A_3/A_{3, B}$; and (dash-dotted line) $A_4/A_{4, B}$. (Top), $\sigma = 0.3$; (bottom) $\sigma = 0.5$; here $A_{3, B} = 0$ therefore only three curves are shown.

Schwarz (13) into which we implemented the Greens' tensor for an elastic layer of finite thickness as detailed in Eqs. 4–11. In the fitting procedure we neglected all deformations measured at distances below 7 μm from the assumed location of the point force. This was necessary because the microstructures could not be tracked to any reasonable accuracy close to and under the needle tip. The fitting procedure yielded convincing results; see Fig. 5. This already indicates that the deformation of an elastomer layer is well described by the Greens' tensor as developed here.

For a more direct comparison we considered the displacements of microstructures along lines through the origin of the point force. We found the results along lines with an inclination of 45° to the direction of the force most instructive. Along these lines, the component of the displacement in direction of force, $u_\parallel$, is given by A_1F and the displacement component perpendicular to the force direction, $u_\perp$, by $-A_2F$; see Eq. 4. In Fig. 6 several examples of displacements along diagonals can be found.

These data clearly show that the deformation fields for thin layers are poorly described by the Boussinesq theory. Above we found from our calculations that the disagreement between finite layer theory and the Boussinesq approach is more serious for A_1 as compared to A_2; cf. Fig. 4. This is also seen in our experimental data, as $u_\parallel$ is proportional to A_1 and $u_\perp$ to A_2. Moreover, whereas the Boussinesq theory is obviously a poor approximation to the displacements measured on thin films, the agreement between data and finite layer theory is quite convincing.
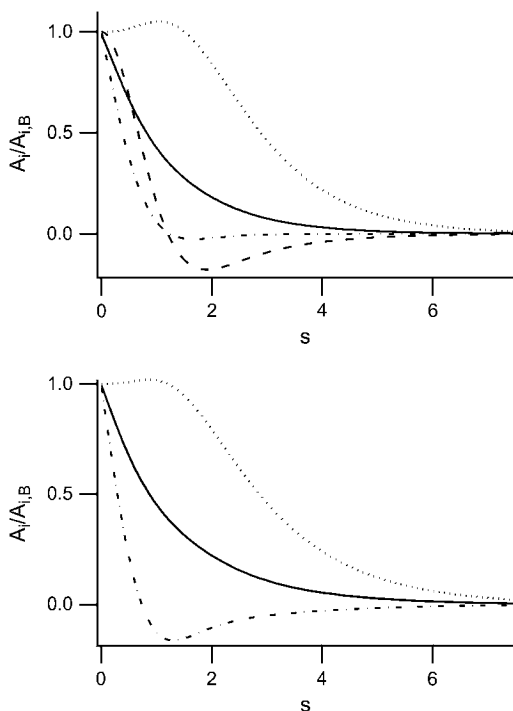
Living cells on different layer thicknesses

Primary cardiac fibroblasts from rat embryos were cultivated on microstructured elastomer films of defined thicknesses. Because we wanted to probe the spatial resolution of traction force microscopy, a very dense pattern of markers for the deformation field was necessary. Using microbead coated elastomer films we were able to achieve a higher density of markers than in the previously described experiments on periodic microstructures.

We evaluated forces of cells cultivated on elastomer films of different thicknesses. For better comparability, force application points for the force fitting algorithm were assigned on a relatively dense regular hexagonal grid. In the data fitting algorithm displacements are calculated for a discrete set of point forces. Under these assumptions, displacements diverge at the points of force application. To deal with these divergences, we ignored displacements at locations closer than 0.25 μm to any site of force application for data fitting. As long as the fraction of removed displacements is small (here below 0.1%), the value of this cutoff distance plays a minor role for the results.
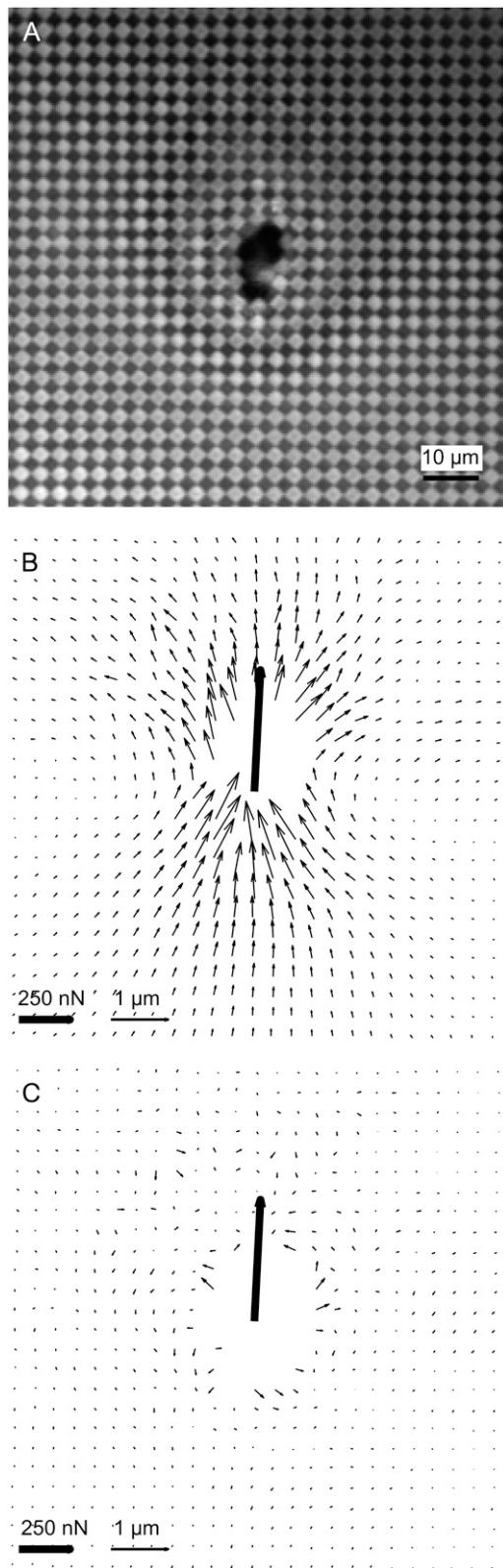
FIGURE 5 Needle deformation test of a 17-μm-thick layer of cross-linked PDMS. (*A*) A micrograph of the sample before deformation. The lattice constant of the microstructure is 3.5 μm. (*B*) The corresponding displacement field. The fat arrow denotes the force applied by the pipette
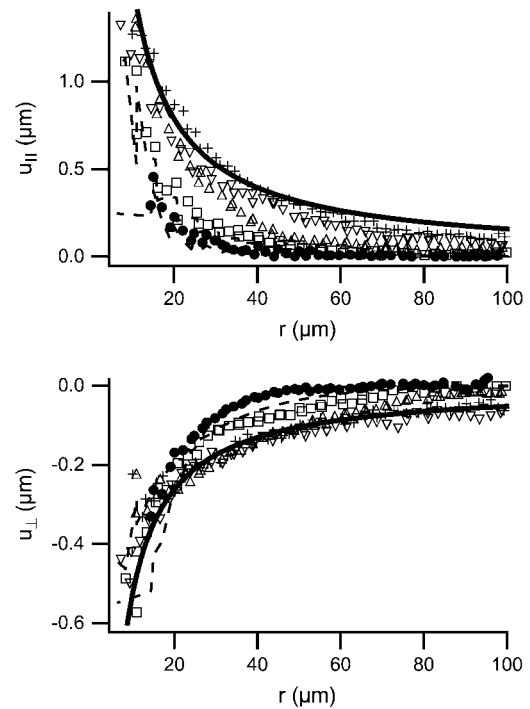

FIGURE 6 Deformation fields of elastomer films along lines inclined by 45° to the force. Shown are the displacements of all points of the microstructure along a 7-μm-wide corridor centered around these diagonals. Layer thicknesses are 8 μm (●), 17 μm (□), 54 μm (△), 84 μm (▽), and 126 μm (+). All deformations were scaled to the mean of the generating forces (0.66 μN), the scaling factors ranged from 0.59 to 1.66. (*Top*) The displacement components along the force direction. (*Bottom*) The displacement components perpendicular to the force direction. In both figures the displacements due to a point force as calculated by the finite layer theory are shown as dashed lines for the two lowest thicknesses. Moreover, the bold lines denote the results of the Boussinesq theory.

Force calculations on thin films showed that the magnitude of the retrieved forces depended strongly on the use of the finite layer theory. Interestingly, force directions depend much less on the use of the correct theory than magnitudes. The results for a cardiac fibroblast cultivated on a 6.6-μm thick elastomer film are displayed in Fig. 7.

A representative image of a cell on relatively thick elastomer substrate is displayed in Fig. 8. Here the force distribution shows much less spatial variation than the one shown in Fig. 7 for a cell on a thin substrate. The same was true for all cells studied. Cell force patterns on thin substrates exhibited stronger spatial variation than those on relatively thick films.

This qualitative observation implies a better spatial resolution of traction force microscopy on thin substrates. However, force calculation involves the choice of a regularization parameter (12,13). This amounts to a trade-off between lateral smoothing of the force field and retrieving erroneously fluctuating forces. Unfortunately, for experiments like the ones presented here where the distribution of the experimental noise was not perfectly Gaussian there is no objective criterion on how to choose the optimum regularization parameter (11). This makes it impossible to quantify the spatial resolution of the force fields in an objective way. Still, analyzing the results of the regularized least squares fit was instructive. For cells on thick substrates, Fig. 9, we obtained results that are more or less typical for numerically ill-posed

(500 nN), the thin arrows the displacements of the dots. Please note the different scalings of space and displacement. (*C*) The deviations between the measured displacements and the ones calculated from the fitted point force.
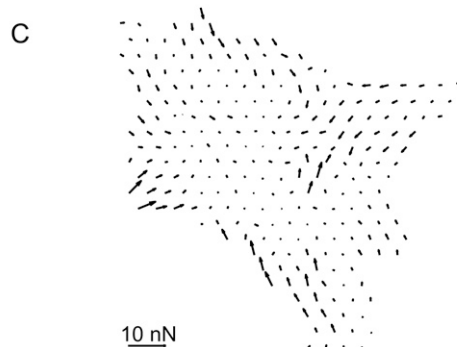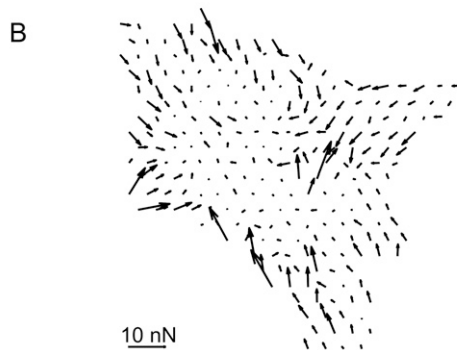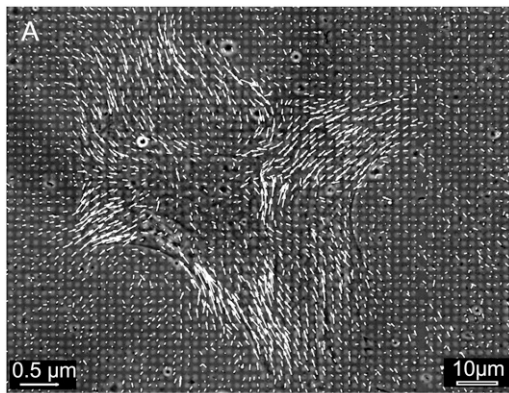
FIGURE 8 A cardiac fibroblast on a 79-μm-thick elastomer film. (*Top*) Reflection image (RICM) of cell and bead displacements (*white arrows*). (*Bottom*) Forces.

FIGURE 7 A cardiac fibroblast on thin elastic substrate (6.6 μm). (*A*) Reflection image (RICM) of the cell and bead displacements (*white arrows*). Note the different scaling of distances and displacements. (*B*) Forces calculated with the finite layer theory. (*C*) Forces evaluated assuming infinite layer thickness.

problems. With increasing regularization parameter λ the normalized χ^2 increased, the constraint C decreased, and in between there was a reasonable compromise to choose the regularization parameter close to the ''knee'' in the double logarithmic plot of constraint C vs. χ^2. In comparison, smaller values of the regularization parameter were sufficient for cells on thin substrates; cf. Fig. 10. Moreover, the ''knee'' in the aforementioned double logarithmic plot was less pronounced indicating less need for regularization for traction force microscopy on thin elastic layers.

Instead of studying force fields to assess the spatial resolution on thin substrates, we analyzed the spatial variations of the measured displacement fields. For this analysis the bead numbers were equalized to 3500 on a field of view of 102 $\times$ 137 μm by removing randomly chosen beads. Subsequently, displacement fields were triangulated to achieve dense fields. After this, spatial resolutions of the resulting fields were down-sampled to 1.6 μm per pixel, close to the mean distance between microbeads. The
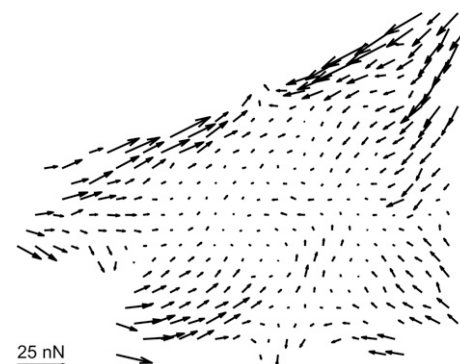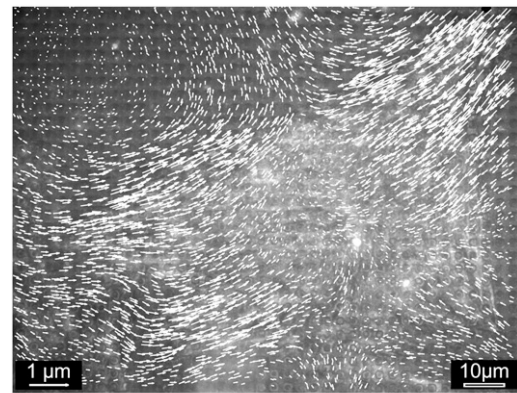
resulting deformation fields were scaled in magnitude by the mean amplitudes of the displacements. Finally the divergences of these normalized deformation fields were calculated. Divergence is a scalar quantity, therefore these data can be displayed as pseudograyscale images. An example is shown in Fig. 11. Although the mean of the divergence over an image was always close to zero, the range of variation depended strongly on film thickness. On substrates ranging in thickness from 79 to 100 μm we found a mean variation of the divergence from -0.022 to 0.020 μm^{-1}. On thin substrates (4.5–9.5 μm thickness) the corresponding variation was -0.062–0.070 μm^{-1}. In all cases the extreme values of the divergence were localized in regions of strong substrate deformation. These results indicate a stronger spatial variation of the deformation field on thin substrates. Therefore we can expect any suitable algorithm for force retrieval to achieve higher spatial resolution on these data.

DISCUSSION

We showed that the deformation field of a point force acting on the surface of an elastic film of finite thickness decays on the length scale of about twice the film thickness; cf. Figs. 3 and 6. Thus the response of an elastic film of finite thickness is more localized than expected by the well-known Boussinesq theory (Eq. 6). As the spatial spread of the material response together with experimental noise in the measured displacement fields limit the spatial resolution of the technique, our finding implies a higher spatial resolution of traction force microscopy on thin substrates. However, this higher resolution
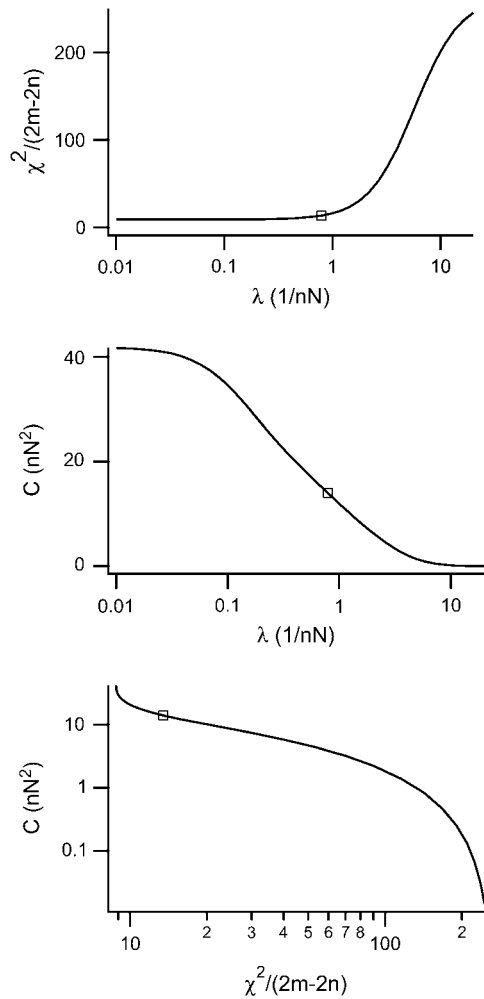
FIGURE 9   Results of the regularized least squares fit algorithm for a cell on a thick elastic substrate (79 μm; same data as in Fig. 8). See Eq. 2 for definitions of the terms. (*Top*) The sum of the squared deviations of the displacement field normalized by the degrees of freedom of the fit $2(m - n)$. (*Middle*) The constraint C, i.e., the sum of the squared forces. (*Bottom*) Variation of C with the normalized χ^2. Open boxes denote the regularization parameter chosen for force retrieval.

FIGURE 10   Results of the regularized least squares fit algorithm for a cell on a thin elastic substrate (6.6 μm; same data as in Fig. 7 *B*). See Eq. 2 for definitions of the terms. (*Top*) The sum of the squared deviations of the displacement field normalized by the degrees of freedom of the fit $2(m - n)$. (*Middle*) The constraint C, i.e., the sum of the squared forces. (*Bottom*) Variation of C with the normalized χ^2. Open boxes denote the regularization parameter chosen for force retrieval.

comes at the expense of reduced displacements; see Fig. 7. Moreover, for a reliable retrieval of forces on the order of 10–100 measured displacement values $\vec{u}_e$ per force to be retrieved are necessary. As the displacement field on thin substrates decays effectively within two layer thicknesses, we were forced to use films whose thicknesses amounted to at least 2–3 times the average distance between marker points. In practice film thicknesses below 4 μm could not be used in our experiments on cells. Yet this still corresponds to a substantial localization of the deformation field of a cell.

Using microneedles we deflected elastic substrates with point forces. We fitted the measured displacement fields using the Boussinesq theory, cf. Eqs. 4 and 6, as well as using the Greens' tensor for finite layer thickness (Eqs. 4 and 7 through 11). The results clearly 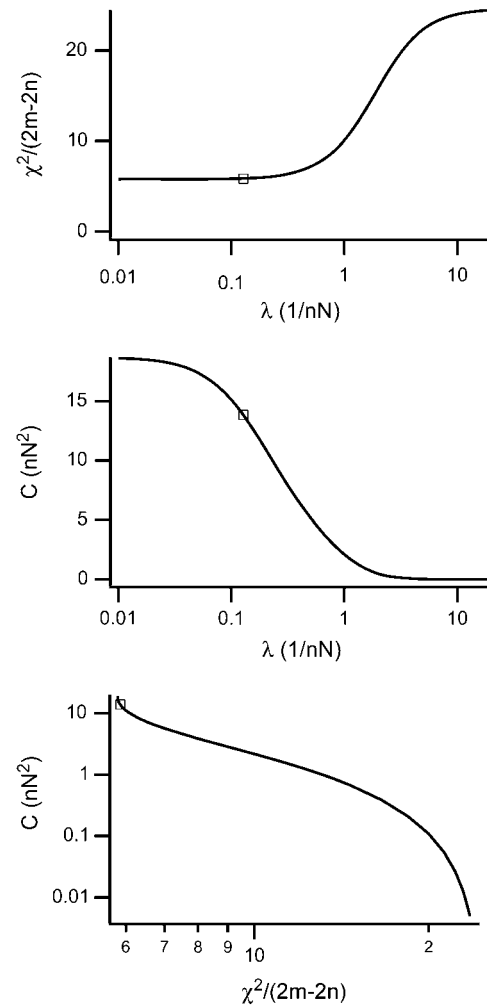indicated a much better description of the data by the finite layer theory. For example, for the data shown in Fig. 5 we calculated the standard deviation of the residual vector field, $\vec{u}_e - \vec{u}_t$, and found values of 0.14 μm for the Boussinesq solution and 0.07 μm for the finite layer solution. These results strongly support the validity of our theory. However, for a rigorous exploration of the spatial resolution of the technique we would need a test sample where forces of some 10 nN are applied on the micrometer length scale in a well-defined manner. All our attempts to construct such a calibration sample failed. Thus we resorted to experiments on living cells and used the spatial variation of the observed displacement vector field as indication for the resolution; cf. Fig. 11. Based on this criterion we found indeed a higher spatial resolution for traction force microscopy on thin elastic substrates.
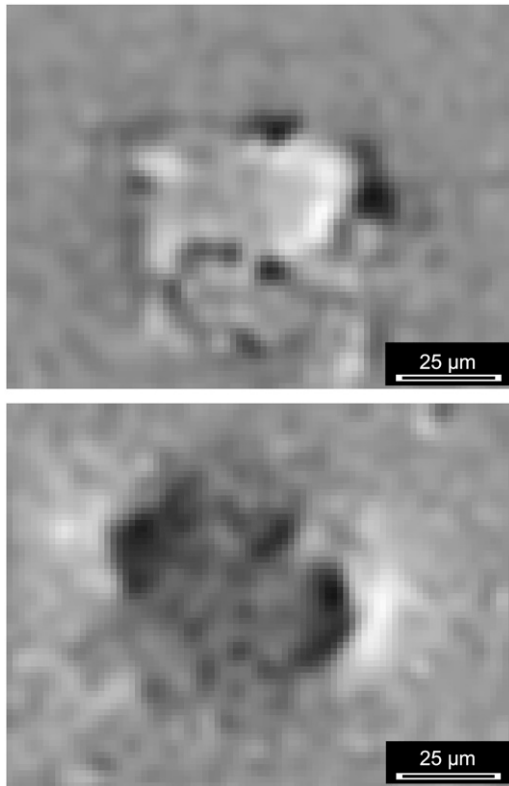
FIGURE 11 Divergences of normalized deformation fields caused by cells. (*Top*) Film thickness 9.5 μm; (*bottom*) film thickness 97 μm. Note the different gray scales: (*top*) from −0.09 1/μm to 0.09 1/μm; (*bottom*) from −0.02 1/μm to 0.02 1/μm.

In addition to improved spatial resolution, we observed that the amount of regularization necessary for force retrieval is less for cells on thin elastic substrates. This is another consequence of the localization of the displacement field due to a point force. Thus using thin elastic films for traction force microscopy might not only increase the spatial resolution of the technique but also improve the robustness of the results against experimental uncertainties.

Besides the possibility to improve the spatial resolution of traction force microscopy our results imply that under imaging conditions as used for eukaryotic cells the deformation field of a point force acting on an elastic film of a thickness of at least 60 μm can be well described by the Boussinesq theory. Therefore one can safely use the established techniques for force retrieval as long as the thickness of the elastic film used is above this limit and the obtainable spatial resolution is sufficient.

Both aspects, localization and reduction of deformations, were clearly visible in simulated data. Here we calculated displacement fields for a mock cell exhibiting ellipsoidal contacts that were uniformly loaded with mechanical forces; cf. Fig. 12. Displacements were calculated using the correct Greens' tensor for film thicknesses of 4.5 and 100 μm, respectively. Uniform loading was modeled by assuming
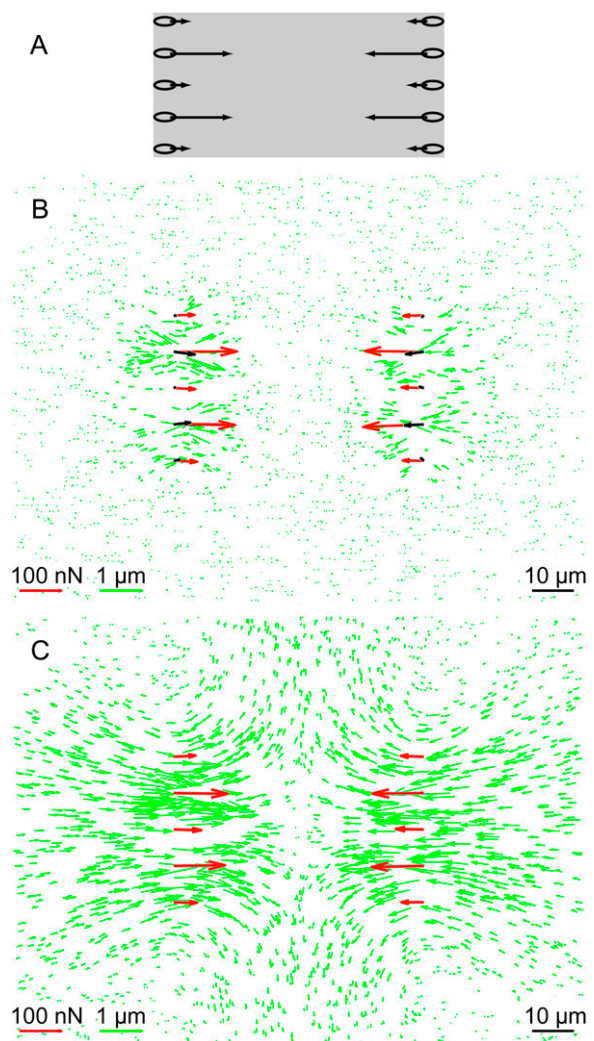

FIGURE 12 Simulated deformation fields. (*A*) The geometry. Forces were applied uniformly over ellipses with 5 μm length and 2 μm width that were equally distributed over the short sides of a 70 × 35 μm sized rectangle. Forces were alternated between 50 and 150 nN. (*B*) Film thickness 4.5 μm. Resulting deformation field (*green arrows*) and retrieved forces assuming the correct thickness (*red arrows*) or infinite layer thickness (*black arrows* with *gray borders*). (*C*) Layer thickness 100 μm. Here forces for correct thickness and infinite thickness coincide. For clarity only 50% of the used displacements are shown in panels *B* and *C*.

200 randomly distributed force application points within each ellipse. Normally distributed noise with a standard deviation of 10 nm was added to the displacements. For force retrieval, point-like forces at the centers of the ellipses were assumed and displacements within 2.5 μm from these points were neglected. For comparison we quote the forces retrieved for the left side of the mock cell from top to bottom. On the right-hand side we obtained very similar results. We used forces of 50, 150, 50, 150, and 50 nN and retrieved 49, 142, 54, 146, and 51 nN on 4.5 μm film thickness assuming the correct thickness of the film. However, on this film thickness the Boussinesq solution yielded forces of 5, 43, 10,

45, and 9 nN. Obviously, the Boussinesq solution is a poor description of these data resulting in severely underestimated forces and high uncertainties even in the ratios of the forces. However, on a film thickness of 100 μm the Boussinesq solution yields correct values that are indistinguishable from the results of the finite layer theory.

Taken together, using elastic layers of 5–10 μm thickness results in higher lateral resolution and improved stability of force retrieval in traction force microscopy. This might prove valuable for studies on cell types with smaller and less separated focal adhesions than typical fibroblasts, the best studied cell type by now. Moreover, on such thin elastic substrates the deformation field more closely resembles the force field than on thick layers. This might open opportunities for screening studies for substances that alter cell forces and cell force patterns. For screening purposes one might be able to omit the time-consuming force retrieval and simply use the deformation field itself as a read-out signal.

REFERENCES

1. Geiger, B., A. Bershadsky, R. Pankov, and K. Yamada. 2001. Transmembrane extracellular matrix—cytoskeleton crosstalk. *Nat. Rev. Mol. Cell Biol.* 2:793–805.

2. Linder, S., and M. Aepfelbacher. 2003. Podosomes: adhesion hot-spots of invasive cells. *Trends Cell Biol.* 13:376–385.

3. Litjens, S., J. de Pereda, and A. Sonnenberg. 2006. Current insights into the formation and breakdown of hemidesmosomes. *Trends Cell Biol.* 16:376–383.

4. Lo, S. 2006. Focal adhesions: what's new inside. *Dev. Biol.* 294:280–291.

5. Harris, A., P. Wild, and D. Stopak. 1980. Silicon rubber substrata: a new wrinkle in the study of cell locomotion. *Science.* 208:177–179.

6. Oliver, T., M. Dembo, and K. Jacobson. 1995. Traction forces in locomoting cells. *Cell Motil. Cytoskeleton.* 31:225–240.

7. Dembo, M., and Y.-L. Wang. 1999. Stresses at the cell-to-substrate interface during locomotion of fibroblasts. *Biophys. J.* 76:2307–2316.

8. Munevar, S., Y.-L. Wang, and M. Dembo. 2001. Traction force microscopy of migrating normal and H-ras transformed 3T3 fibroblasts. *Biophys. J.* 80:1744–1757.

9. Balaban, N., U. Schwarz, D. Riveline, P. Goichberg, G. Tzur, I. Sabanay, D. Mahalu, S. Safran, A. Bershadsky, L. Addadi, and B. Geiger. 2001. Force and focal adhesion assembly: a close relationship studied using elastic micropatterned substrates. *Nat. Cell Biol.* 3:466–472.

10. Butler, J., I. Tolić-Nørrelykke, B. Fabry, and J. Fredberg. 1991. Traction fields, moments, and strain energy that cells exert on their surroundings. *Am. J. Physiol. Cell Physiol.* 282:C595–C605.

11. Press, W., S. Teukolsky, W. Vettering, and B. Flannery. 2002. Numerical Recipes in C++. The Art of Scientific Computing. Cambridge University Press, Cambridge, UK.

12. Dembo, M., T. Oliver, A. Ishihara, and K. Jacobson. 1996. Imaging the traction stresses exerted by locomoting cells with the elastic substratum method. *Biophys. J.* 70:2008–2022.

13. Schwarz, U., N. Balaban, D. Riveline, A. Bershadsky, B. Geiger, and S. A. Safran. 2002. Calculation of forces at focal adhesions from elastic substrate data: the effect of localized force and the need for regularization. *Biophys. J.* 83:1380–1394.

14. Cesa, C., N. Kirchgeßner, D. Mayer, U. Schwarz, B. Hoffmann, and R. Merkel. 2007. Micropatterned silicon elastomer for high resolution analysis of cell force patterns. *Rev. Sci. Instrum.* 78:034301-1–034301-10.

15. Hansen, P. 1994. Regularization tools: a Matlab package for analysis and solution of discrete ill-posed problems. *Numer. Algorithms.* 6:1–35.

16. Pawley, J. 2006. Handbook of Biological Confocal Microscopy. Springer Science + Business Media, New York.

17. Boussinesq, J. 1885. Application des potentiels à l'étude de l'équilibre et du mouvement des solides élastiques. Gauthier-Villars, Paris, France.

18. Burmister, D. 1945. The general theory of stresses and displacements in layered systems. I. *J. Appl. Phys.* 16:89–94.

19. Burmister, D. 1945. The general theory of stresses and displacements in layered soil systems. II. *J. Appl. Phys.* 16:126–127.

20. Burmister, D. 1945. The general theory of stresses and displacements in layered soil systems. III. *J. Appl. Phys.* 16:296–302.

21. Yue, Z. 1995. On generalized Kelvin solutions in a multilayered elastic medium. *J. Elast.* 40:1–43.

22. Yue, Z. Q. 1996. On elastostatics of multilayered solids subjected to general surface traction. *Quarterly Journal of Mechanics and Applied Mathematics.* 49:471–499.

23. Yue, Z., J.-H. Yin, and S.-Y. Zhang. 1999. Computation of point load solutions for geo-materials exhibiting elastic non-homogeneity with depth. *Computers and Geotechnics.* 25:75–105.

24. Ai, Z., Z. Yue, L. Tham, and M. Yang. 2002. Extended Sneddon and Muki solutions for multilayered elastic materials. *Int. J. Eng. Sci.* 40:1453–1483.

25. Schwarzer, N. 2000. Arbitrary load distribution on a layered half space. *Transactions of the ASME.* 122:672–681.

26. Abramowitz, M., and I. Stegun. 1964. Handbook of Mathematical Functions. National Bureau of Standards, Washington, DC.